ACCOUNTS of chemical research

pubs.acs.org/accounts Article

A Look Inside the Black Box of Machine Learning Photodynamics Simulations

Jingbai Li and Steven A. Lopez*

Cite This: *Acc. Chem. Res.* 2022, 55, 1972−1984 Read Online

ACCESS | Metrics & More | Article Recommendations | Supporting Information

CONSPECTUS: Photochemical reactions are of great importance in chemistry, biology, and materials science because they take advantage of a renewable energy source, mild reaction conditions, and high atom economy. Light absorption can excite molecules to a higher energy electronic state of the same spin multiplicity. The following nonadiabatic processes induce molecular transformations that afford exotic molecular architectures and high-energy-isomers that are inaccessible by thermal means. Computational simulations now complement time-resolved instrumentation to reveal ultrafast excited-state mechanistic information for photochemical reactions that is essential in disentangling elusive spectroscopic features, excited-state lifetimes, and excited-state mechanistic critical points. Nonadiabatic molecular dynamics (NAMD), powered by surface hopping techniques, is among the most widely applied techniques to model the photochemical reactions of medium-sized molecules. However, the computational efficiency is limited because of the requisite thousands of multiconfigurational quantum-chemical calculations multiplied by hundreds of trajectories. Machine learning (ML) has emerged as a revolutionary force in computational chemistry to predict the outcome of the resource-intensive multiconfigurational calculations on the fly. An ML potential trained with a substantial set of quantum-chemical calculations can predict the energies and forces with errors under chemical accuracy at a negligible cost. The integration of ML potentials in NAMD dramatically extends the maximum simulation time scale by ∼10 000-fold to the nanosecond regime.

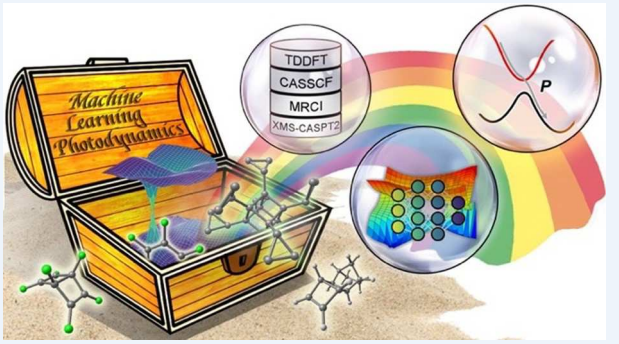

In this Account, we present a comprehensive demonstration of ML photodynamics simulations and summarize our most recent applications in resolving complex photochemical reactions. First, we address three fundamental components of ML techniques for photodynamics simulations: the quantum-chemical data set, the ML potential, and NAMD. Second, we describe best practices in building training data and our procedure toward training the ML photodynamics model with our recent literature contributions. We introduce a convenient training data generation scheme combining Wigner sampling and geometrical interpolation. It trains reliable and effective ML potentials suitable for subsequent active learning to detect undersampled data. We demonstrate how active learning automatically discovers new mechanistic pathways and reproduces experimental results. We point out that atomic permutation is an essential data augmentation approach to improve the learnability of distance-based molecular descriptors for highly symmetric molecules. Third, we demonstrate the utility of ML-photodynamics by showing the results of ML photodynamics simulations of (1) photo-torquoselective 4π disrotatory electrocyclic ring closing of norbornyl cyclohexadiene, which reveals a thermal conversion from experimentally unobserved intermediates to the reactant in 1 ns; (2) [2 + 2] photocycloaddition of substituted [3]-*syn*-ladderdienes in competition with 4π and 6π electrocyclic ring-opening reactions, uncovering substituent effects to explain the reported increased quantum yield of substituted cubane precursors; and (3) photochemical 4π disrotatory electrocyclic reactions of fluorobenzenes in nanoseconds with XMS-CASPT2-level training data. We expect this Account to broaden understanding of ML photodynamics and inspire future developments and applications to increasingly large molecules within complex environments on long time scales.

KEY REFERENCES

- Li, J.; Reiser, P.; Boswell, B. R.; Eberhard, A.; Burns, N. Z.; Friederich, P.; Lopez, S. A. Automatic discovery of photoisomerization mechanisms with nanosecond machine learning photodynamics simulations. *Chem. Sci.* **2021**, *12*, 5302−5314.[1] *This article presents our first implementation of the machine learning photodynamics code Python Rapid Artificial Intelligence Ab Initio*

Received: May 9, 2022
Published: July 7, 2022

https://doi.org/10.1021/acs.accounts.2c00288
Acc. Chem. Res. 2022, 55, 1972−1984

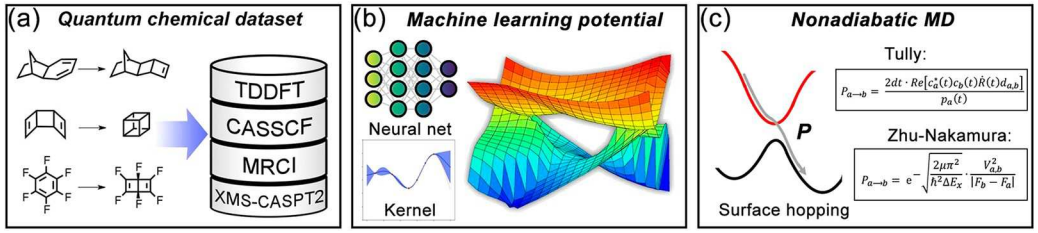

Figure 1. Three components of the ML photodynamics approach. (a) The QC data set stores the information on photochemical reactions. (b) ML algorithms learn excited-state potential energy surfaces. (c) NAMD is used to propagate trajectories using the ML potential.

Molecular Dynamics (PyRAI²MD) and demonstrates the role of nanosecond-scale photodynamics simulations in resolving the photo-torquoselectivity observed in experiments.

- Li, J.; Stein, R.; Adrion, D. M.; Lopez, S. A. Machine-Learning Photodynamics Simulations Uncover the Role of Substituent Effects on the Photochemical Formation of Cubanes. *J. Am. Chem. Soc.* **2021**, *143*, 20166−20175.[2] *This work showcases the advantages of machine learning photodynamics simulations for complex photochemical reactions that uncover the substituent effects on the photochemical [2 + 2] cycloaddition toward octasubstituted cubane.*
- Li, J.; Lopez, S. A. Excited-state distortions promote the photochemical 4π-disrotatory electrocyclizations of fluorobenzenes via machine learning accelerated photodynamics simulations. *Chem. - Eur. J.* **2022**, DOI: 10.1002/chem.202200651.[3] *This work demonstrates the significance of machine learning photodynamics simulations for revealing the long-lived nonradiative decay mechanism of fluorobenzenes and its role in the photochemical formation of Dewar-fluorobenzenes.*

1. INTRODUCTION

Photochemistry is appealing because it harnesses renewable solar energy to synthesize chemical products[4] and fuels[5−8] under mild conditions with a high atomic conversion efficiency. Photochemical reactions occur via radiationless processes on an ultrashort time scale (10^{-15}−10^{-12} s). The mechanism studies rely on time-resolved experiments (i.e., attochemistry[9]) to probe the excited-state molecular vibrations and electronic structures. Comprehensive investigations are complemented with computational modeling to disentangle the elusive spectroscopic features and identify the critical excited-state structures. Quantum-chemical (QC) calculations for excited-state electronic structures are often costly. Therefore, machine learning (ML) techniques have been introduced to accelerate the calculations.

ML models learn the relationship between molecular structures and associated properties (e.g., energies,[10−13] transition dipole moments,[10−13] and oscillator strengths[14,15]) from a large QC data set. The applications have succeeded in the discovery of new molecules[16] and materials,[17] predicting reaction barriers,[18] finding transition states,[19,20] solving the Schrödinger equation,[21,22] modeling wave functions,[23,24] optimizing density functionals,[25,26] computing IR spectra,[27] UV−vis spectra,[11,13] and NMR spectra,[28] and simulating excited-state dynamics[12,29] and complex photochemical reactions.[1−3] The energy prediction achieves chemical accuracy (1 kcal·mol^{-1}), which is required for realistic chemical prediction and comparison with experiments. The costs are negligible compared with the same-level QC calculation.[12,29] Thus, many studies have used ML potentials as a prominent accelerator for nonadiabatic molecular dynamics (NAMD) simulations, for instance, multiconfigurational time-dependent Hartree (MCTDH)[30] and trajectory surface hopping (TSH)[31] calculations. Several groups have developed ML mixed quantum−classical NAMD approaches (called ML photodynamics in this Account), such as MLAtom[32] with Newton-X[33] and SchNarc[34] with SHARC.[35] To study photochemical cycloaddition and electrocyclic reactions, our group developed the Python Rapid Artificial Intelligence Ab Initio Molecular Dynamics (PyRAI²MD) code.[1]

Training ML potentials is a challenging task. First, generating high-quality machine-learnable QC data requires expertise in computational chemistry and ML. The training data generation protocol often inherits human biases that require specific steps to remove. Second, the rapid development of ML models has made comparing the efficiencies and performances of these models rather challenging.[36] We begin with an overview of the fundamental background for ML photodynamics. We will then provide a short tutorial on building ML potentials and discuss the applications in our recent publications. Finally, we will summarize our findings and outlook on future method development.

2. THE ML PHOTODYNAMICS APPROACH

ML photodynamics methods generally contain three key components (Figure 1): the QC data set, the ML potential, and NAMD.

2.1. Quantum-Chemical Data Set for Training

Single-reference methods (e.g., time-dependent density functional theory) are used to compute vertical excitation energies with an errors ranging from 0.3 to 0.5 eV.[37] However, they fail when there is strong coupling between electronic states (e.g., avoided crossings or conical intersections) because it violates the Born−Oppenheimer approximation. Single-reference methods may also predict incorrect branching-plane dimensionality at these crossing regions.[38,39] Multiconfigurational self-consistent field (MCSCF) methods, such as complete active space self-consistent field (CASSCF), are more suitable for describing the electronic structures near the crossing regions. The term CASSCF(m, n) refers to an active space of m electrons and n orbitals. The CASSCF wave function is often limited to an active space of 22 electrons and 22 orbitals with modern quantum-chemical software.[40] The selection of active orbitals is not trivial. Active spaces that are too small may cause high-lying state(s) to become relatively low-lying along the reaction coordinate, known as intruder state(s). Accounting for electron correlation significantly improves the energies, which can approach the experimental energies. The correlation

https://doi.org/10.1021/acs.accounts.2c00288
Acc. Chem. Res. 2022, 55, 1972−1984

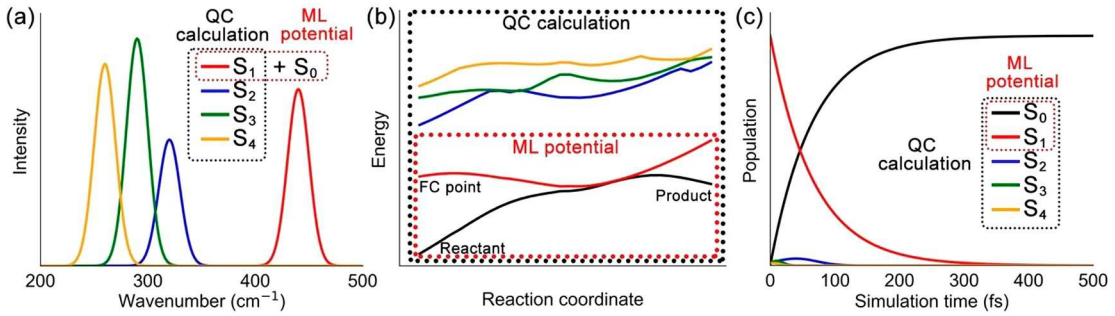

Figure 2. Three perspectives of selecting electronic states on the basis of (a) the absorption spectrum, (b) the reaction coordinate diagram, and (c) state populations from QC-NAMD simulations.

energy is divided into static and dynamic components. CASSCF recovers the static correlation by its multideterminant formalism. However, it omits dynamic correlation because it treats each electron in the mean field of the other electrons. Thus, it usually results in overestimated excitation energies.[41] The use of CASSCF data must be carefully validated against multireference methods, such as multireference configuration interaction (MRCI) and extended multistate complete active space second-order perturbation theory (XMS-CASPT2). We recommend the ANO-type double-ζ basis set or comparable aug-cc-pVDZ basis set because they provide a balance between computational cost and accuracy and capture diverse excitation types, including Rydberg states.[42,43] Moreover, Bowan, Lester, and co-workers showed that in the dissociation of CH_3COO Criegee intermediates[44] and more recently Marquet and and co-workers showed that in the dissociation of tyrosine,[45] there are no available reference methods can describe the entire reaction space, requiring a combination of QC methods to be employed.

2.2. Machine Learning Potentials

Kernel methods and neural networks (NNs) are the two most common methods to train ML potentials. Various examples are high-dimensional neural network potential (HDNNP),[46] SchNet,[47] PhysNet,[48] ANI,[49] deep potential smooth edition (DeepPot-SE),[50] gradient-domain machine learning (GDML),[51] kernel ridge regression using RE descriptor and the Gaussian kernel (KREG),[32] reproducing kernel Hilbert space (RKHS),[52] and Gaussian approximation potential (GAP).[53] Some packages of a collection of ML methods are MLatom[32] and fast learning of atomic rare events (FLARE).[54] A comparison of NN and kernel methods shows rather similar accuracies for ML photodynamics simulations.[55] We refer readers to refs 12 and 32 for more information about the method benchmarks. Our following discussion will focus on the most basic architecture of NNs based on fully connected feed-forward multilayer perceptrons.

ML potentials predict molecular properties using a numerical representation of the 3D molecular structure. Global descriptors contain complete molecular structural information, such as the so-called Coulomb matrix[56] and inverse distance matrix.[10] They are translation- and rotation-invariant and thus can distinguish molecular structures in arbitrary orientations and positions. However, global descriptors are not invariant to permuted chemically equivalent atoms. Specialized techniques (e.g., bag of bonds,[57] randomly sorted Coulomb matrices,[58] and permutationally invariant polynomials[59]) are introduced to enforce permutation invariance in global descriptors. However, these techniques may apply only to small molecules and result in discontinuous potential energy surfaces (PESs). On the other hand, local descriptors describe atomistic environments with a set of basis functions[12,36] that are permutationally invariant. However, they may introduce system-dependent hyperparameters (e.g., shape and size of the basis functions). Some examples are atom-centered symmetry functions (ACSFs),[60] smooth overlap of atomic positions (SOAP),[61] and Faber−Christensen−Huang−Lilienfeld (FCHL).[62] In addition, Pozdnyakov and co-workers suggested that the inclusion of higher-order terms in descriptors is essential to further improve the model accuracy.[63] The ML potentials are often trained for a specific molecule in ML photodynamics.[12] Thus, we implemented global descriptors (e.g., inverse distance matrix) in PyRAI^{2}MD for simplicity. We enable more efficient training through a data augmentation approach (see section 3.4).

Many databases, such as GDB-13[64] and GDB-17[65] and their subsets QM7,[66] QM7b,[67] QM8,[68] and QM9[15] as well as the VERDE materials database,[69] are designed to learn molecular properties at equilibrium geometries. However, ML photodynamics relies on a more specialized dataset that contains the molecular properties at different geometries for a given molecule. Active learning is an efficient and practical strategy for this task. It allows models to sample undersampled data resembling an automatic reaction exploration. We will discuss the initial set generation in section 3.2 and active learning in section 3.3.

2.3. Nonadiabatic Molecular Dynamics

The ML photodynamics approach is based on mixed quantum−classical NAMD using TSH methods, such as Tully's fewest switches surface hopping (FSSH). It computes the hopping probability between two states of the same spin multiplicity with the nonadiabatic couplings (NACs) and spin−orbit couplings (SOCs) for different spin multiplicities.[70] It is more challenging to predict NACs than SOCs because NACs are vector properties. Marquetand and co-workers suggested that fitting numerator components of NACs to the first-order-derivative of a virtual potential[71] avoids the discontinuous data near state crossings. Recent work by our group[1] and the Gómez-Bombarelli group[72] showed that the NNs tend to underestimate NACs with increasing atom count because of the unavailability of training data for the unphysical virtual potential and/or low-accuracy predictions of energy gaps near crossing regions. A possible solution to the NAC prediction problem is to use the Baeck-An approximation based on the ML-predicted energies.[34,73] The improvement of the energy gap is challenging and requires substantial

https://doi.org/10.1021/acs.accounts.2c00288
Acc. Chem. Res. 2022, 55, 1972−1984

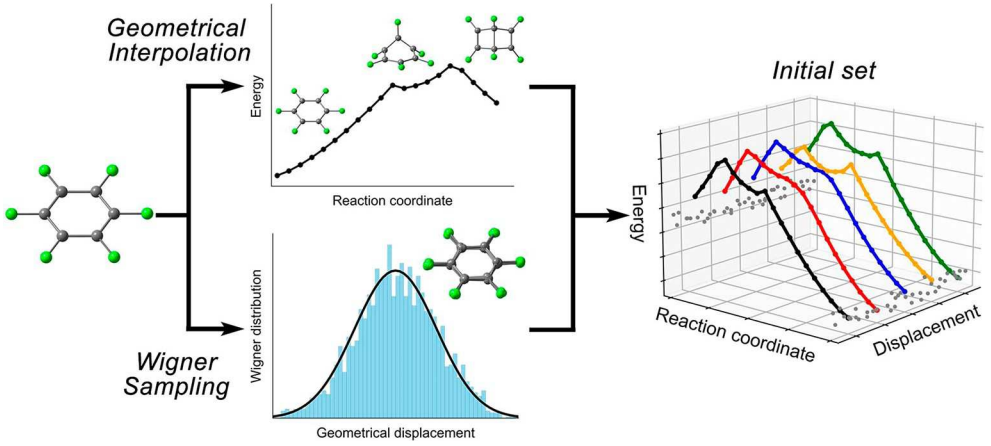

Figure 3. Initial set generation with geometrical interpolation and Wigner sampling. The colored curves represent the interpolated points, and the gray points represent the Wigner-sampled reactant and product structures.

computational effort to generate data near crossing regions. The NAC prediction may be bypassed with the Zhu–Nakamura theory of surface hopping (ZNSH).[74] ZNSH uses only energies and forces of two crossing states in hopping probability calculations. The forces are diabatized in a generalized 1D model based on three-point interpolation.[75] ZNSH has shown results consistent with those of FSSH.[75−77] It also has a formula to compute intersystem crossing with SOCs.[78] Our examples in section 4 used ZNSH. Since the ZNSH solely depends on the shape of the PESs, one must justify the ZNSH results with FSSH if the QC-NAMD data are available. In addition, the recent developments of ML methods for multiscale systems[79] and long-range dispersion[80] in the ground-state potential pave the way to the future ML photodynamics approach for larger systems.

3. TRAINING ML PHOTODYNAMICS MODELS

3.1. Building an ML Potential

We first determine an appropriate number of electronic states to construct an ML potential. It is recommended to first compute the absorption spectrum and compare with available experimental results to assess relevant states in the excitation (Figure 2a). The reaction coordinate diagram is also useful to characterize the selected states along with a possible reaction path (Figure 2b). A more rigorous justification requires analyzing the state populations during QC-NAMD simulations (Figure 2c). Because the model system in Figure 2 shows a separate S_1 and higher states in the absorption spectrum and reaction diagram and the state population transfer mainly involves the S_1 and S_0 states, we can build an ML potential to learn the S_0 and S_1 energies and forces, which reduces the dataset size and training noise.

Training an ML potential minimizes a mean-square-error loss function using gradient descent methods.[81] We split the training data into two parts (e.g., 9:1). The first part is used to train the model; the other part is for test or validation. The kernel methods and NNs may contain hyperparameters that need additional optimization, which can be done with grid search and random grid search.[82] With a limited amount of training data, *k*-fold cross-validation is an effective approach for hyperparameter optimization.[83] NN potentials are prone to overfitting, where the model fits the training data and noise generally leads to predictive failure outside the training set. Thus, we recommend overfitting prevention (e.g., early stopping, dropout, and weight decay).[82,84] Early stopping stops the training procedure when the validation error increases while the training error decreases. Dropout randomly ignores the outputs from some number of nodes to prevent complex coadaptation of nodes within the layer, making a more robust prediction. Weight decay adds a small penalty to the loss function to prevent overfitting.

3.2. Initial Set Sampling

Initial set sampling provides a baseline for learning the PESs. Structural sampling has been done in thermal reactions with MD-based methods (umbrella sampling,[85] trajectory-guided sampling,[86] enhanced sampling,[87] and metadynamics[88]), stochastic surface walk,[89] Wigner sampling,[90] and normal mode scans.[71,91] However, these techniques have limited efficacy for complex photochemical reactions. For instance, Wigner sampling for reactant or product geometries captures only accessible nonequilibrium geometries near local or global minima. Normal mode scans include many irrelevant molecular vibrations; ground-state MD simulations access different mechanistic pathways from excited-state processes. Excited-state MD becomes prohibitively expensive as the number of degrees of freedom increases. We recently reported a composite scheme that combines Wigner sampling and geometrical interpolation to generate a compact yet relevant initial set (Figure 3).

Wigner sampling is commonly used to generate initial conditions for photodynamics and absorption spectra.[92] Learning the Wigner-sampled reactants helps reduce the undersampling of structures near the Franck–Condon (FC) region. Geometrical interpolation complements structural correlations between the reactants and products in the dataset. We use geodesic interpolation[93] to generate intermediate structures between the optimized reactant, product, and minimum-energy crossing point (MECP) geometries. We combine the Wigner-sampled geometrical displacements of reactants with the interpolated structures to broaden the sampled space (Figure 3). For sampling structures of larger systems in a complex environment, Wigner sampling needs to be combined with multiscale MD simulations to sample the environment.[94]

We train five models to demonstrate the effect of Wigner sampling and geometrical interpolation. Each model consists of two independently trained NNs. The hyperparameters and training results are available in the Supporting Information. We

https://doi.org/10.1021/acs.accounts.2c00288
Acc. Chem. Res. 2022, 55, 1972−1984

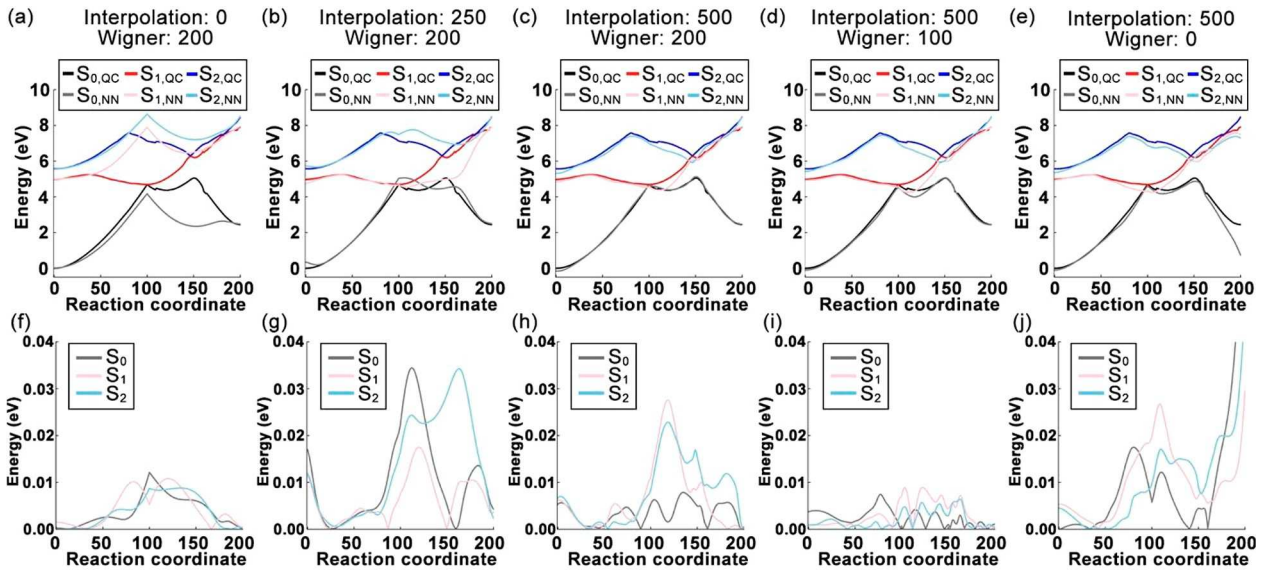

Figure 4. (a–e) NN-predicted reaction coordinate diagrams for various sizes of the Wigner and interpolations sets. (f–j) Uncertainties of the NN-predicted S_0, S_1, and S_2 energies. The predicted energy is the average of the results from two independently trained NNs. The uncertainty is the standard deviation of the two NN predictions. Training data calculations were performed at the XMS-CASPT2(6,7)/aug-cc-pVDZ level.

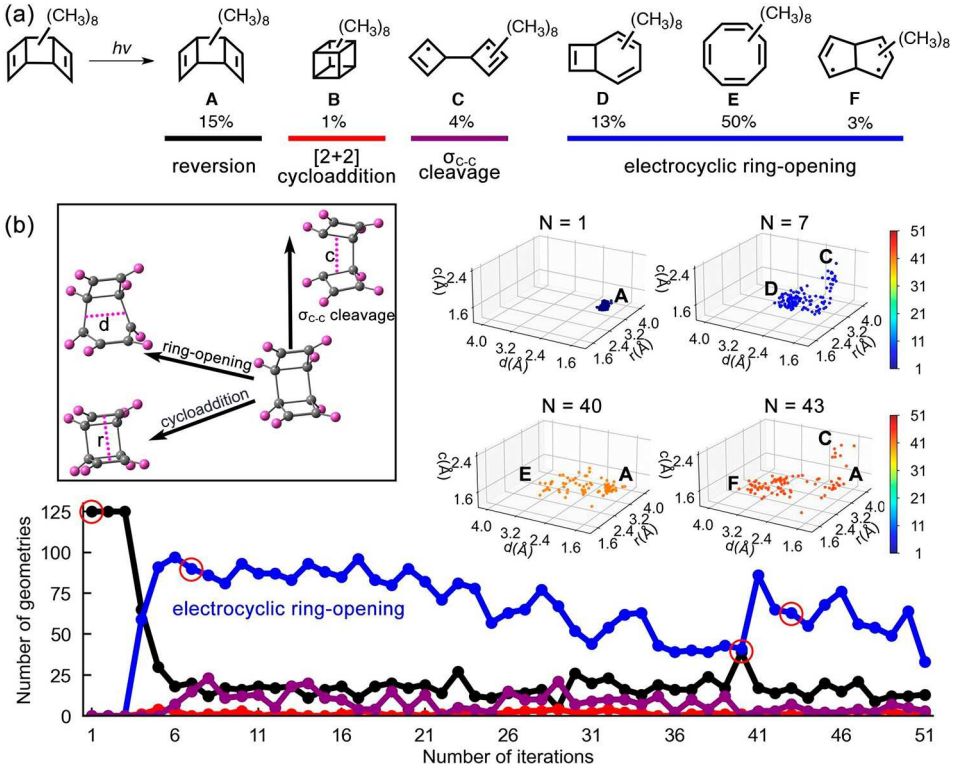

Figure 5. (a) NN-predicted photochemical reactions of octamethyl-[3]-ladderdiene and yields. (b) Plots of the number of collected structures of octamethyl-[3]-ladderdiene as a function of active learning iteration. The legend shows the reaction space defined by the three reaction coordinates *r*, *d*, and *c*, corresponding to the [2 + 2] cycloaddition, electrocyclic ring-opening, and σ_{C-C} cleavage pathways, respectively. The inset 3D plots illustrate the spatial distributions of the collected structures.

use the prediction standard deviations to estimate the prediction uncertainties. The training set is built upon two subsets in varying ratios: the Wigner sampling set contains 100 reactant and product structures, and the geometrical interpolation set contains 500 structures (25 paths by 20 intermediates). The test set has 201 interpolated structures in the 4π disrotatory electrocyclization of hexafluorobenzene (HFB).

Figure 4a shows that the NNs exclusively trained with the Wigner set predict the incorrect topology of PESs near the S_1/S_0 crossing region. The prediction uncertainty rises to >0.01 hartree (>6.2 kcal mol^{-1}), which suggests an area of undersampled structures (Figure 4f). Upon addition of 50%

https://doi.org/10.1021/acs.accounts.2c00288
Acc. Chem. Res. 2022, 55, 1972–1984

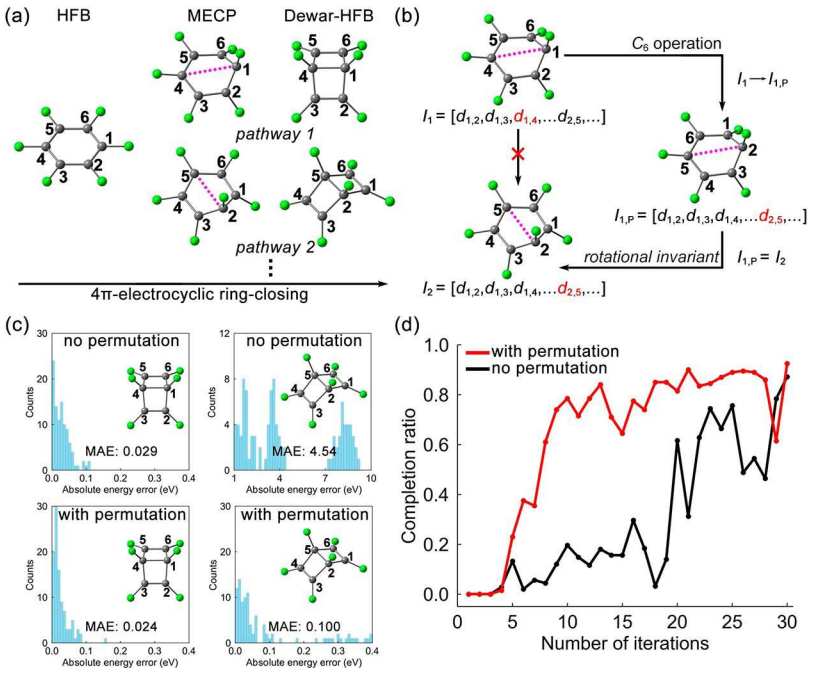

Figure 6. (a) Two chemically equivalent pathways in the 4π disrotatory electrocyclization of HFB. (b) Permutation map for HFB, defined by the "C_6 operation" reordering the atoms around the C_6 axis of HFB. (c) NN-predicted energies of Dewar-HFB with and without the permutation map. The left column is the control set, and the right column is the test set. (d) Active learning curves of HFB with and without a permutation map. The completion ratio is the number of complete trajectories divided by the total number of trajectories.

of the interpolation set, the NNs learn the S_1/S_0 crossing but predict two crossing regions (Figure 4b) and show high uncertainty (>0.03 hartree) near the S_1/S_0 and S_2/S_1 crossings (Figure 4g). Including the complete interpolation set predicts a better topology throughout the reaction coordinate diagram (Figure 4c). The uncertain regions narrow to the S_0/S_1 crossing (Figure 4h). Reducing the Wigner set by 50% shows similar errors near the S_1/S_0 crossing region (Figure 4d). However, the uncertainty decreases below 0.01 hartree, which makes the model less effective in detecting undersampled structures (Figure 4i). As can be seen in Figure 4e, removing the Wigner set results in notable uncertainty, especially for the product (Figure 4j). Our findings suggest equal significance of Wigner sampling and geometrical interpolation in the initial set generation but do not yet indicate an optimal ratio between the Wigner and interpolation sets.

3.3. Active Learning

Active learning, which searches undersampled structures in the initial set, was initially introduced by Behler[95] for ground-state MD simulations and then adapted for excited-state PESs by Marquetand and co-workers.[71] Active learning uses a similarity measure to determine the uncertainty of predicted molecular properties during MD simulations. Kernel-based methods (e.g., Gaussian process regression) may provide the covariance of the predictions as an estimate of the prediction uncertainty. However, the NN potential needs a committee model of at least two independently trained NNs to evaluate uncertainties. The ML potential is first trained with the initial set and propagates an ensemble of trajectories to search undersampled structures. These trajectories are terminated if the predicted energies, forces, NACs, and SOCs of the current structures exceed predefined thresholds (e.g., 0.043 hartree and 0.25 hartree·bohr^{-1} for energy and force, respectively).[1,2] The uncertain structures are recomputed with QC calculations and added to retrain the ML potential.

Our recent ML photodynamics simulations for octamethyl-[3]-ladderdiene (**A**) showed substantial efficacy of active learning in the automatic discovery of new reaction pathways.[2] The initial training set contained only 4321 structures sampled from the interpolated reaction coordinate diagram for the [2 + 2] cycloaddition. The active learning propagated 125 trajectories from the S_1 state in 1 ps (0.5 fs time step). It completed in 51 iterations and found 4982 new structures from the σ_{C-C} cleavage and electrocyclic ring-opening pathways with five predicted intermediates or products (Figure 5a). In Figure 5b, we have plotted the number of collected structures and their distributions to visualize the learning progress in the reaction space. In the first three iterations, the trajectories searched around the FC region (**A**, r > 2.0 Å, d < 2.0 Å, and c < 2.0 Å). A broader exploration began at iteration 7 that learned the electrocyclic ring-opening pathways to **D** and **E** (r > 2.0 Å, d > 2.0 Å, and c < 2.0 Å), and the σ_{C-C}-cleavage pathways to **C** (r > 2.0 Å, d < 2.0 Å, and c > 2.0 Å). The undersampled structures in the electrocyclic ring-opening pathway gradually decreased to a plateau at iterations 36−40. After that, the trajectories detected a new pathway toward **F** (r > 2.0 Å, d > 3.2 Å, and c < 2.0 Å).

3.4. Data Augmentation

Symmetric molecules render the inverse distance matrix unable to learn the photochemical reaction pathways. For instance, HFB (D_{6h} symmetry) undergoes a 4π disrotatory electrocyclization reaction. It has six equivalent carbons (Figure 6a). Active learning tends to search all equivalent reaction pathways because the inverse distance matrix is not permutationally invariant. This increases the training data calculations ~6-fold. To reduce these redundant QC calculations, we introduced a data augmentation approach, called a permutation map, to

https://doi.org/10.1021/acs.accounts.2c00288
Acc. Chem. Res. 2022, 55, 1972−1984

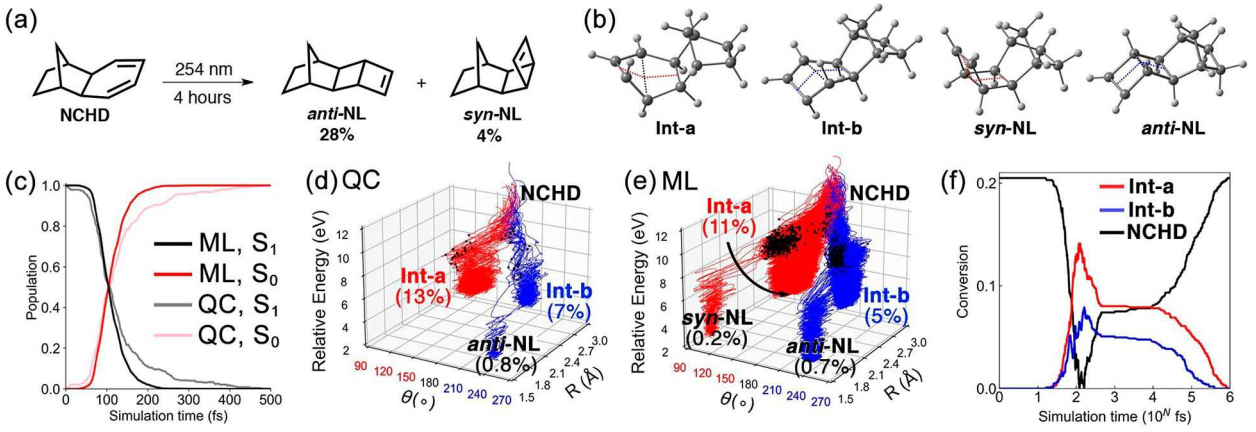

Figure 7. (a) Photo-torquoselective isomerization of norbornyl cyclohexadiene (**NCHD**). (b) Geometries of intermediates and products optimized at the CASSCF(4,3)/ANO-S-VDZP level. The red and blue dotted lines highlight the angle θ in the syn and anti configurations. The black dotted lines show the distance R. (c) State populations of the 240 QC and 3954 ML trajectories. (d) QC and (e) ML trajectories of **NCHD** in 1 ps simulations at 300 K. The black dots represent the last surface hopping point in each trajectory. (f) Conversion between **NCHD** and **Int-a** and **Int-b** in 1 ns. From ref 1. CC BY-NC 3.0.

generate equivalent data from existing data. In Figure 6b, pathways 1 and 2 have equivalent MECPs with different representations, I_1 and I_2. The permutation maps reorder the atoms of the MECP in pathway 1 around the C_6 axis of HFB. The permuted MECP has a new representation $I_{1,P}$, and $I_{1,P} = I_2$ because the inverse distance matrix is rotationally invariant. Since the permutation map reorders the atoms in the representation, all of the vector properties (e.g., forces and NACs) are also reordered accordingly.

We compare the predicted energies of Dewar-HFB with and without permutations to show the significance of our data augmentation approach. Details of the NN hyperparameters and training results are given in the Supporting Information. The training set contains the 901 structures from Wigner sampling and geometrical interpolation of the C1−C4 bond formation.[3] The control set contains 100 Dewar-HFB structures with the C1−C4 bond. The predictions show similar error distributions regardless of the permutations (Figure 6c). The test set contains 100 Dewar-HFB structures with the C2−C5 bond. Without permutations, the predictions result in a large mean absolute error (MAE) of 4.54 eV. Using the permutation map, however, decreases the MAE to 0.100 eV. Figure 6d compares the progress of the direct active learning approach with that of active learning with an HFB permutation map. It propagates 200 trajectories from S_1 in 10 ps (0.5 fs time step). In the active learning with permutations, the completion ratio reaches 0.8 in 10 iterations and exceeds 0.9 in 30 iterations. Without permutations, the learning curve fluctuates in the first 20 iterations and requires 29 iterations to reach a 0.8 completion ratio. The active learning with permutations collects considerably fewer structures (2128) than that without permutations (3029). The data augmentation can be avoided using a permutationally invariant local descriptor, such the descriptor implemented in SchNarc.[34]

4. APPLICATIONS OF ML PHOTODYNAMICS SIMULATIONS

In this section, we provide an overview of our latest contributions in applying ML photodynamics to resolve mechanistic problems in photochemistry. Photochemical cycloaddition and electrocyclic reactions serve as fundamental routes to produce highly strained organic compounds that are typically inaccessible via thermal routes. CASSCF or XMS-CASPT2 calculations were used as reference methods to properly describe the PESs involving state degeneracies along the reaction coordinate(s). However, the demonstrated systems all require substantial—sometimes prohibitive—computational costs for large molecules or reactions that have excited-state lifetimes exceeding 10 ps. ML photodynamics simulations enable the acceleration of energy and gradient predictions on increasingly large molecules.

4.1. Photo-torquoselective Isomerization of Norbornyl Cyclohexadiene

Irradiation of norbornyl cyclohexadiene (**NCHD**) initiates a torquoselective 4π disrotatory electrocyclic ring-closing reaction to major (*anti*-**NL**) and minor (*syn*-**NL**) norbornyl ladderene (**NL**) products (Figure 7a).[1] We performed QC and ML photodynamics simulations to uncover the origin of the photo-torquoselectivity. We computed 240 QC trajectories of **NCHD** at the CASSCF(4,3)/ANO-S-VDZP level and 3954 ML trajectories with NNs trained at the same level in 1 ps. The QC trajectory required 17 days, whereas the ML trajectory only took 38 s on a single CPU. The final MD snapshots were optimized to intermediates and products (Figure 7b).

The ML trajectories show excited-state dynamics and an S_1 half-life consistent with those from the QC trajectories (Figure 7c). They predict a 0.2% quantum yield of *syn*-**NL** (Figure 7e), which is missing in the QC trajectories because of the limited number of trajectories (Figure 7d). The ML photodynamics simulations are consistent with our PES calculations and confirm that the syn pathway is steeper than the anti pathway, forming a higher ratio of **Int-a**. However, the anti pathway has a steeper energy descent at the S_1/S_0 crossing seam, favoring *anti*-**NL**. The 984 1 ns ML trajectories reveal thermal conversions from the unexpected intermediates **Int-a** and **Int-b** to **NCHD** (Figure 7f), which explains their absence in the experiment. This work demonstrates the efficiency and accuracy of ML photodynamics simulations and emphasizes the importance of long-time-scale simulations.

4.2. Substituent Effects on the Photochemical Reactions of [3]-Ladderdiene

The [2 + 2] cycloaddition of [3]-ladderdienes can access cubanes. The quantum yield of cubane increases in the [3]-

https://doi.org/10.1021/acs.accounts.2c00288
Acc. Chem. Res. 2022, 55, 1972−1984

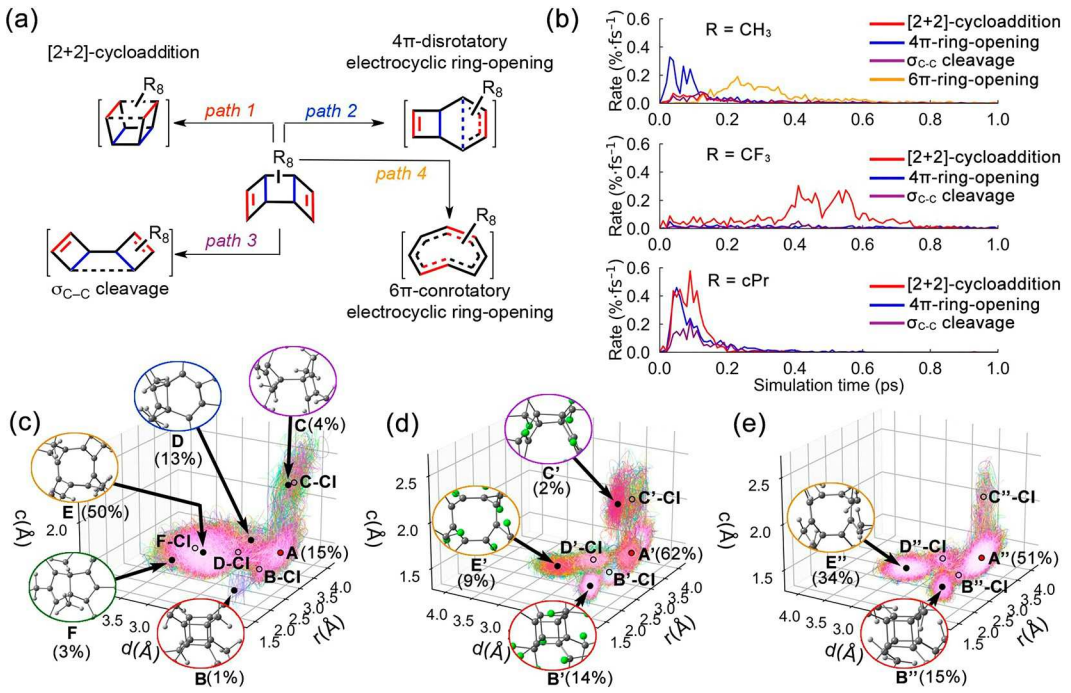

Figure 8. (a) NN-predicted relaxation pathways of octamethyl, octatrifluoromethyl, and octacyclopropyl [3]-ladderdiene. (b) NN-simulated relaxation rates of substituted [3]-ladderdienes. (c–e) NN trajectories of (c) CH_3-, (d) CF_3-, and (e) cPr-substituted [3]-ladderdiene. Each plot contains 400 randomly selected trajectories. The averaged starting points, surface hopping points, and products are marked with red dots, black circles, and black dots, respectively. The inset legends illustrate the last trajectory snapshot with predicted yields. Reproduced from ref 2. Copyright 2021 American Chemical Society.

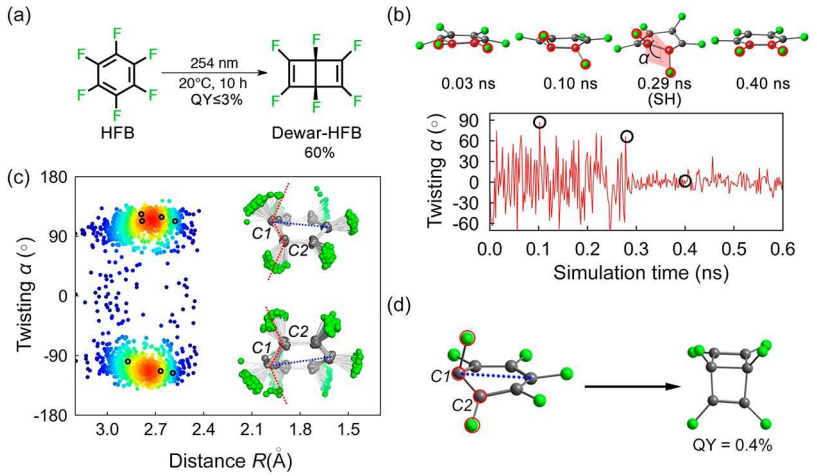

Figure 9. (a) Photochemical 4π disrotatory electrocyclization of HFB. (b) A trajectory reversing to HFB in the first 0.6 ns simulations. It traces the twisting angle α in a 2 ps interval, highlighted by the red circles on the structures. The black circles mark the twisting angle in each snapshot. (c) Structural distribution of the HFB hopping points. The scatter points are defined by the twisting angle α (highlighted in red dotted lines) and the 1,4-carbon distance R (marked by blue dotted lines), shown in the aligned hopping structures. The colors from blue to red represent the accumulation of the hopping points from low to high, as evaluated by Gaussian kernel density estimation. The black circles mark the hopping points undergoing 4π disrotatory electrocyclization. (d) An HFB hopping structure leads to the 4π disrotatory electrocyclization. Reproduced with permission from ref 3. Copyright 2022 Wiley-VCH.

ladderdienes octasubstituted with methyl (CH_3), trifluoromethyl (CF_3), and cyclopropyl (cPr) groups.[2] We recently performed the first simulations for these molecules using ML photodynamics.[2] The NNs were trained with CASSCF(8,7)/ANO-S-VDZP+ANO-S-MB (for substituents) calculations. The trajectories were propagated from the S_1 FC region for 2 ps (0.5 fs time step). We collected 3835, 3259, and 3122 trajectories for octamethyl (**A**), octatrifluoromethy (**A′**), and octacyclopropyl [3]-ladderdiene (**A″**) to analyze the excited-state dynamics. Figure 8a,b illustrates the observed pathways and $S_1 \rightarrow S_0$ relaxation half-lifes.

The ML trajectories discovered four S_1 relaxation pathways in the trajectories of octamethyl [3]-ladderdiene: (1) [2 + 2] cycloaddition, (2) 4π disrotatory electrocyclic ring opening, (3) σ_{C-C} cleavage, and (4) 6π conrotatory electrocyclic ring opening. The 4π and 6π ring-opening reactions have higher relaxation rates than the [2 + 2] cycloaddition (Figure 8b). The closed-shell repulsion in CF_3 blocks the 6π ring-opening

https://doi.org/10.1021/acs.accounts.2c00288
Acc. Chem. Res. 2022, 55, 1972−1984

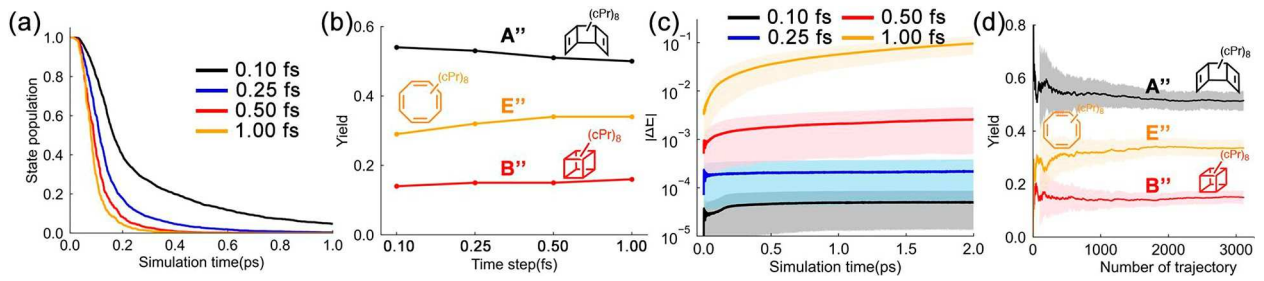

Figure 10. (a) S_1 state population, (b) product distributions, and (c) energy conservation in the ML photodynamics simulation of **A″** with Δt = 1, 0.5, 0.25, and 0.10 fs. (d) Predicted yields as functions of the number of trajectories of **A″**. The shaded areas in (c) and (d) denote the range of one standard deviation obtained from bootstrapping 10% of the total trajectories 100 times. Panel (d) was adapted from ref 2. Copyright 2021 American Chemical Society.

pathway, enhancing the [2 + 2] cycloaddition. The steric effect of cPr also accelerates the [2 + 2] cycloaddition reaction to compete with the 4π disrotatory electrocyclic ring-opening reaction. Figure 8c shows a broad trajectory distribution toward five products, where the quantum yield of octamethyl cubane is 1%. As can be seen in Figure 8d,e, the steric clashes narrow the spatial distributions of the reaction paths and deactivate the side-reaction channels. These findings explain the increasing quantum yields of octatrifluoromethyl (14%) and octacyclopropyl cubane (15%). This work highlights the capability of ML photodynamics simulations to discover complex photochemical reactions.

4.3. Photocyclization of Hexafluorobenzenes

Hexafluorination of benzene significantly enhances the chemoselectivity of the photochemical 4π disrotatory electrocyclization to strained Dewar-HFB (Figure 9a).[96] However, the long-lived nonradiative decay of HFB and low quantuam yield of Dewar-HFB prevent productive QC-NAMD simulations from understanding the mechanisms.[96] The ML photodynamics simulations enable us to model the excited-state dynamics of HFB in 4 ns at the XMS-CASPT2(6,7)/aug-cc-pVDZ level.[3]

The ML photodynamics simulations show that most HFBs reform the reactant. Figure 9b illustrates one of the HFB trajectories in the first 600 ps (0.6 ns). The snapshots display the pseudo-Jahn−Teller distortions breaking the planar structure with out-of-plane C−F bending. The nonradiative decay occurs at a surface hopping point involving a π_{C-C} cis−trans isomerization, where the twisting angle α is 110° at 0.29 ns. Figure 9c plots the distribution of the HFB hopping points. The hopping structures reveal a smooth twisting of the C−F bonds around the C1−C2 bond, indicating a continuous S_1/S_0 crossing seam. However, the structures leading to the 4π disrotatory electrocyclization are sparsely distributed along the seam without a particular clustering pattern (R = 2.58−2.87 Å). This implies that neither the π_{C-C} twisting nor the 1,4-carbon distance directly determines the formation of Dewar-HFB. Thus, the 4π disrotatory electrocyclization of HFB could be attributed to the dynamical effects in the post-surface-hopping structures, with the nuclear momentum continuously populating the bond-forming vibration mode. Figure 9d shows a surface hopping point yielding Dewar-fluorobenzene. The predicted reaction quantum yield is 0.3%, in line with the experimental results (≤3%).[97]

4.4. Remarks on ML Photodynamics Simulations

Long-time-scale ML photodynamics simulations extensively integrate Newton's equation of motion. The time step strongly depends on the vibrational frequency of the system under investigation. For instance, a typical vibrational period of C−H stretching in small organic molecules is about 10 fs, suggesting that the maximum time step should be 1 fs. A time step that is too large may accumulate substantial errors in trajectory propagations. The simulations also require a sufficient number of trajectories to meet the statistical convergence of the considered properties (e.g., time constants and quantum yields). However, this information is often unavailable in QC-NAMD studies because of the computational cost. In this subsection, we use ML photodynamics simulations to explore the influence of the integration time step and number of trajectories on simulation of photochemical reactions. The model system is octacyclopropyl [3]-ladderdiene (**A″**).

The trajectories were propagated from the S_1 in 1 ps. We collected 3266, 3268, 3271, and 3211 trajectories with time steps (Δt) of 0.1, 0.25, 0.5, and 1 fs, respectively. Figure 10a plots the time evolution of the S_1 population. For Δt = 0.1 fs, the predicted S_1 half-life is 165.6 fs. Increasing the step size to 1 fs shortens the half-life to 80 fs. However, the product distributions are less sensitive than the state populations. Setting Δt from 0.1 to 1 fs lowers the yield of **A″** only from 0.54 to 0.50 and increases the yield of **B″** from 0.14 to 0.16 and the yield of **E″** from 0.29 to 0.34 (Figure 10b). A recent benchmark by Barbatti and co-workers reported that the random numerical noise of 10^{-5} hartree in energy calculations at Δt = 0.5 fs causes the total energy not to be conserved in NAMD simulations.[98] As the NN potential is trained at chemical accuracy (1.6×10^{-3} hartree), the choice of Δt needs extra carefulness. For Δt = 0.1 fs, the trajectories obtain reasonable energy conservation with an absolute energy drift of 5×10^{-5} hartree (Figure 10c). The energy drifts increase to 2×10^{-4} and 2×10^{-3} hartree at Δt = 0.25 and 0.5 fs, respectively. However, Δt = 1 fs accumulates a tremendous energy drift approaching 0.1 hartree in 2 ps of simulation. Thus, we think that Δt = 0.5 fs is required for energy conservation in ML photodynamics.

Figure 10d plots the predicted yields as functions of the number of trajectories of **A″**. A typical 500 trajectories that we usually consider in QC-NAMD simulations do not predict a converged yield. The yields significantly fluctuate under 1000 trajectories. Thus, the ML photodynamics simulations require at least 1100−1500 trajectories to reach statistical convergence.

5. CONCLUSIONS AND OUTLOOK

We have presented an overview of ML-photodynamics and demonstrated its value in resolving the role of substituent effects on the reactivities, stereoselectivities, and automatically

https://doi.org/10.1021/acs.accounts.2c00288
Acc. Chem. Res. 2022, 55, 1972−1984

identifying mechanistic pathways with active learning in photochemical reactions. We combined Wigner sampling and geometrical interpolation to simplify training data generation. The method trains effective ML potentials to predict qualitatively correct PESs and detect undersampled structures near crossing regions. Moreover, we discussed data augmentation with atomic permutations that mitigate the permutational variance in the inverse distance matrix representation; it substantially accelerates active learning for photochemical reactions of high-symmetry molecules.

ML photodynamics enables highly efficient nanosecond NAMD simulations with the quality of CASSCF and XMS-CASPT2 for relatively large molecules. The training requires minimal prior knowledge of the intended photochemical reaction. The current limitations of ML photodynamics are unsatisfactory predictions of NACs and the energy gaps near the crossing regions. Current ML photodynamics simulations may employ NAC-free surface hopping methods such as the Zhu−Nakamura theory until a more suitable model for NAC predictions is developed. Overall, ML photodynamics simulations provide a valuable tool to study long-time-scale photochemical reactions. We expect this Account to contribute to a deeper understanding of the ML photodynamics approach and inspire future applications in simulating photochemistry in molecular solids and explicit solvation with further applications in chemical biology and materials chemistry, solid-state, explicit-solvent, and biological systems.

■ ASSOCIATED CONTENT

Supporting Information

The Supporting Information is available free of charge at https://pubs.acs.org/doi/10.1021/acs.accounts.2c00288.

NN hyperparameters, training metrics, and data availability (PDF)

■ AUTHOR INFORMATION

Corresponding Author

Steven A. Lopez − *Department of Chemistry and Chemical Biology, Northeastern University, Boston, Massachusetts 02115, United States;* orcid.org/0000-0002-8418-3638; Email: s.lopez@northeastern.edu

Author

Jingbai Li − *Department of Chemistry and Chemical Biology, Northeastern University, Boston, Massachusetts 02115, United States*

Complete contact information is available at: https://pubs.acs.org/10.1021/acs.accounts.2c00288

Notes

The authors declare no competing financial interest.

Biographies

Jingbai Li received his Ph.D. in 2019 from the Illinois Institute of Technology, working with Prof. Andrey Yu. Rogachev. He was a postdoctoral researcher at Northeastern University, working with Prof. Steven A. Lopez and developed PyRAI^{2}MD in the Lopez group. He is an associate professor in the Hoffmann Institute of Advanced Materials at Shenzhen Polytechnic. His research is focused on development of ML-photodynamics approaches for studying photochemical reactions in complex environments.

Steven A. Lopez earned his Ph.D. in 2015 from the University of California, Los Angeles, working with Prof. Kendall N. Houk. He was a DOE Energy Efficiency and Renewable Energy Postdoctoral Fellow at Harvard University, working with Prof. Alán Aspuru-Guzik. He is an assistant professor in the Chemistry & Chemical Biology Department at Northeastern University. His group is focused on understanding light-driven processes in organic molecules and soft materials using state-of-the-art QC methods and ML techniques.

■ ACKNOWLEDGMENTS

J.L. and S.A.L. acknowledge the Office of Naval Research (N00014-18-1-2659) National Science Foundation (CAREER Grant NSF-CHE-2144556), and the National Science Foundation (NSF-OAC-2118201) for funding this research. J.L. and S.A.L. appreciate the assistance from the Northeastern Research Computing Team and the computing resources provided by the Massachusetts Life Science Center (Grant G00006360).

■ REFERENCES

(1) Li, J.; Reiser, P.; Boswell, B. R.; Eberhard, A.; Burns, N. Z.; Friederich, P.; Lopez, S. A. Automatic discovery of photoisomerization mechanisms with nanosecond machine learning photodynamics simulations. *Chem. Sci.* **2021**, *12* (14), 5302−5314.

(2) Li, J.; Stein, R.; Adrion, D. M.; Lopez, S. A. Machine-Learning Photodynamics Simulations Uncover the Role of Substituent Effects on the Photochemical Formation of Cubanes. *J. Am. Chem. Soc.* **2021**, *143* (48), 20166−20175.

(3) Li, J.; Lopez, S. A. Excited-State Distortions Promote the Photochemical 4π-Electrocyclizations of Fluorobenzenes via Machine Learning Accelerated Photodynamics Simulations. *Chem. - Eur. J.* **2022**, DOI: 10.1002/chem.202200651.

(4) *Solar-to-Chemical Conversion: Photocatalytic and Photoelectrochemical Processes*; Sun, H., Ed.; Wiley, 2021.

(5) de Meijere, A.; Redlich, S.; Frank, D.; Magull, J.; Hofmeister, A.; Menzel, H.; Konig, B.; Svoboda, J. Octacyclopropylcubane and some of its isomers. *Angew. Chem., Int. Ed. Engl.* **2007**, *46* (24), 4574−6.

(6) Xie, J.; Zhang, X.; Shi, C.; Pan, L.; Hou, F.; Nie, G.; Xie, J.; Liu, Q.; Zou, J.-J. Self-photosensitized [2 + 2] cycloaddition for synthesis of high-energy-density fuels. *Sustainable Energy & Fuels* **2020**, *4* (2), 911−920.

(7) Dong, L.; Feng, Y.; Wang, L.; Feng, W. Azobenzene-based solar thermal fuels: design, properties, and applications. *Chem. Soc. Rev.* **2018**, *47* (19), 7339−7368.

(8) Orrego-Hernandez, J.; Dreos, A.; Moth-Poulsen, K. Engineering of Norbornadiene/Quadricyclane Photoswitches for Molecular Solar Thermal Energy Storage Applications. *Acc. Chem. Res.* **2020**, *53* (8), 1478−1487.

(9) Merritt, I. C. D.; Jacquemin, D.; Vacher, M. Attochemistry: Is Controlling Electrons the Future of Photochemistry? *J. Phys. Chem. Lett.* **2021**, *12* (34), 8404−8415.

(10) Westermayr, J.; Gastegger, M.; Menger, M.; Mai, S.; Gonzalez, L.; Marquetand, P. Machine learning enables long time scale molecular photodynamics simulations. *Chem. Sci.* **2019**, *10* (35), 8100−8107.

(11) Westermayr, J.; Marquetand, P. Deep learning for UV absorption spectra with SchNarc: First steps toward transferability in chemical compound space. *J. Chem. Phys.* **2020**, *153* (15), 154112.

(12) Westermayr, J.; Marquetand, P. Machine Learning for Electronically Excited States of Molecules. *Chem. Rev.* **2021**, *121* (16), 9873−9926.

(13) Westermayr, J.; Maurer, R. J. Physically inspired deep learning of molecular excitations and photoemission spectra. *Chem. Sci.* **2021**, *12* (32), 10755−10764.

(14) Pronobis, W.; Schütt, K. T.; Tkatchenko, A.; Müller, K.-R. Capturing intensive and extensive DFT/TDDFT molecular properties with machine learning. *Eur. Phys. J. B* **2018**, *91* (8), No. 178.

(15) Ramakrishnan, R.; Hartmann, M.; Tapavicza, E.; von Lilienfeld, O. A. Electronic spectra from TDDFT and machine learning in chemical space. *J. Chem. Phys.* **2015**, *143* (8), No. 084111.
(16) Nandy, A.; Duan, C.; Taylor, M. G.; Liu, F.; Steeves, A. H.; Kulik, H. J. Computational Discovery of Transition-metal Complexes: From High-throughput Screening to Machine Learning. *Chem. Rev.* **2021**, *121* (16), 9927−10000.
(17) Friederich, P.; Hase, F.; Proppe, J.; Aspuru-Guzik, A. Machine-learned potentials for next-generation matter simulations. *Nat. Mater.* **2021**, *20* (6), 750−761.
(18) Lewis-Atwell, T.; Townsend, P. A.; Grayson, M. N. Machine learning activation energies of chemical reactions. *Wiley Interdiscip. Rev.: Comput. Mol. Sci.* **2021**, DOI: 10.1002/wcms.1593.
(19) Peterson, A. A. Acceleration of saddle-point searches with machine learning. *J. Chem. Phys.* **2016**, *145* (7), No. 074106.
(20) Pozun, Z. D.; Hansen, K.; Sheppard, D.; Rupp, M.; Muller, K. R.; Henkelman, G. Optimizing transition states via kernel-based machine learning. *J. Chem. Phys.* **2012**, *136* (17), 174101.
(21) Hermann, J.; Schatzle, Z.; Noe, F. Deep-neural-network solution of the electronic Schrodinger equation. *Nat. Chem.* **2020**, *12* (10), 891−897.
(22) Han, J.; Zhang, L.; E, W. Solving many-electron Schrödinger equation using deep neural networks. *J. Comput. Phys.* **2019**, *399*, No. 108929.
(23) Schutt, K. T.; Gastegger, M.; Tkatchenko, A.; Muller, K. R.; Maurer, R. J. Unifying machine learning and quantum chemistry with a deep neural network for molecular wavefunctions. *Nat. Commun.* **2019**, *10* (1), 5024.
(24) Gastegger, M.; McSloy, A.; Luya, M.; Schutt, K. T.; Maurer, R. J. A deep neural network for molecular wave functions in quasi-atomic minimal basis representation. *J. Chem. Phys.* **2020**, *153* (4), No. 044123.
(25) Zhou, Y.; Wu, J.; Chen, S.; Chen, G. Toward the Exact Exchange-Correlation Potential: A Three-Dimensional Convolutional Neural Network Construct. *J. Phys. Chem. Lett.* **2019**, *10* (22), 7264−7269.
(26) Dick, S.; Fernandez-Serra, M. Machine learning accurate exchange and correlation functionals of the electronic density. *Nat. Commun.* **2020**, *11* (1), 3509.
(27) Gastegger, M.; Behler, J.; Marquetand, P. Machine learning molecular dynamics for the simulation of infrared spectra. *Chem. Sci.* **2017**, *8* (10), 6924−6935.
(28) Gao, P.; Zhang, J.; Peng, Q.; Zhang, J.; Glezakou, V. A. General Protocol for the Accurate Prediction of Molecular (13)C/(1)H NMR Chemical Shifts via Machine Learning Augmented DFT. *J. Chem. Inf. Model.* **2020**, *60* (8), 3746−3754.
(29) Dral, P. O.; Barbatti, M. Molecular excited states through a machine learning lens. *Nat. Rev. Chem.* **2021**, *5*, 388−405.
(30) Bonfanti, M.; Worth, G. A.; Burghardt, I. Multi-Configuration Time-Dependent Hartree Methods: From Quantum to Semiclassical and Quantum-Classical. In *Quantum Chemistry and Dynamics of Excited States: Methods and Applications*; González, L., Lindh, R., Eds.; Wiley, 2021; pp 383−411.
(31) Mai, S.; Marquetand, P.; González, L. Surface Hopping Molecular Dynamics. In *Quantum Chemistry and Dynamics of Excited States: Methods and Applications*; González, L., Lindh, R., Eds.; Wiley, 2021; pp 499−530.
(32) Dral, P. O.; Ge, F.; Xue, B. X.; Hou, Y. F.; Pinheiro, M., Jr.; Huang, J.; Barbatti, M. MLatom 2: An Integrative Platform for Atomistic Machine Learning. *Top Curr. Chem.* **2021**, *379* (4), 27.
(33) Barbatti, M.; Ruckenbauer, M.; Plasser, F.; Pittner, J.; Granucci, G.; Persico, M.; Lischka, H. Newton-X: a surface-hopping program for nonadiabatic molecular dynamics. *Wiley Interdiscip. Rev. Comput. Mol. Sci.* **2014**, *4* (1), 26−33.
(34) Westermayr, J.; Gastegger, M.; Marquetand, P. Combining SchNet and SHARC: The SchNarc Machine Learning Approach for Excited-State Dynamics. *J. Phys. Chem. Lett.* **2020**, *11* (10), 3828−3834.
(35) Mai, S.; Marquetand, P.; Gonzalez, L. Nonadiabatic dynamics: The SHARC approach. *Wiley Interdiscip. Rev.: Comput. Mol. Sci.* **2018**, *8* (6), e1370.
(36) Pinheiro, M., Jr.; Ge, F.; Ferre, N.; Dral, P. O.; Barbatti, M. Choosing the right molecular machine learning potential. *Chem. Sci.* **2021**, *12* (43), 14396−14413.
(37) Huix-Rotllant, M.; Ferré, N.; Barbatti, M. Time-Dependent Density Functional Theory. In *Quantum Chemistry and Dynamics of Excited States: Methods and Applications*; González, L., Lindh, R., Eds.; Wiley, 2021; pp 13−46.
(38) Huix-Rotllant, M.; Nikiforov, A.; Thiel, W.; Filatov, M. Description of Conical Intersections with Density Functional Methods. *Top Curr. Chem.* **2015**, *368*, 445−76.
(39) Levine, B. G.; Ko, C.; Quenneville, J.; MartÍnez, T. J. Conical intersections and double excitations in time-dependent density functional theory. *Mol. Phys.* **2006**, *104* (5−7), 1039−1051.
(40) Vogiatzis, K. D.; Ma, D.; Olsen, J.; Gagliardi, L.; de Jong, W. A. Pushing configuration-interaction to the limit: Towards massively parallel MCSCF calculations. *J. Chem. Phys.* **2017**, *147* (18), 184111.
(41) Helmich-Paris, B. Benchmarks for Electronically Excited States with CASSCF Methods. *J. Chem. Theory Comput.* **2019**, *15* (7), 4170−4179.
(42) Gomez, S.; Ibele, L. M.; Gonzalez, L. The 3s Rydberg state as a doorway state in the ultrafast dynamics of 1,1-difluoroethylene. *Phys. Chem. Chem. Phys.* **2019**, *21* (9), 4871−4878.
(43) Roos, B. O.; Merchan, M.; McDiarmid, R.; Xing, X. Theoretical and Experimental Determination of the Electronic Spectrum of Norbornadiene. *J. Am. Chem. Soc.* **1994**, *116* (13), 5927−5936.
(44) Kidwell, N. M.; Li, H.; Wang, X.; Bowman, J. M.; Lester, M. I. Unimolecular dissociation dynamics of vibrationally activated CH_3CHOO Criegee intermediates to OH radical products. *Nat. Chem.* **2016**, *8* (5), 509−14.
(45) Westermayr, J.; Gastegger, M.; Vörös, D.; Panzenboeck, L.; Joerg, F.; González, L.; Marquetand, P. Deep learning study of tyrosine reveals that roaming can lead to photodamage. *Nat. Chem.* **2022**, DOI: 10.1038/s41557-022-00950-z.
(46) Behler, J. Four Generations of High-Dimensional Neural Network Potentials. *Chem. Rev.* **2021**, *121* (16), 10037−10072.
(47) Schutt, K. T.; Sauceda, H. E.; Kindermans, P. J.; Tkatchenko, A.; Muller, K. R. SchNet - A deep learning architecture for molecules and materials. *J. Chem. Phys.* **2018**, *148* (24), 241722.
(48) Unke, O. T.; Meuwly, M. PhysNet: A Neural Network for Predicting Energies, Forces, Dipole Moments, and Partial Charges. *J. Chem. Theory Comput.* **2019**, *15* (6), 3678−3693.
(49) Gao, X.; Ramezanghorbani, F.; Isayev, O.; Smith, J. S.; Roitberg, A. E. TorchANI: A Free and Open Source PyTorch-Based Deep Learning Implementation of the ANI Neural Network Potentials. *J. Chem. Inf. Model.* **2020**, *60* (7), 3408−3415.
(50) Zhang, L.; Han, J.; Wang, H.; Saidi, W. A.; Car, R.; Weinan, E. End-to-end symmetry preserving inter-atomic potential energy model for finite and extended systems. In *Proceedings of the 32nd International Conference on Neural Information Processing Systems*; Curran Associates, 2018; pp 4441−4451.
(51) Chmiela, S.; Sauceda, H. E.; Muller, K. R.; Tkatchenko, A. Towards exact molecular dynamics simulations with machine-learned force fields. *Nat. Commun.* **2018**, *9* (1), 3887.
(52) Koner, D.; Meuwly, M. Permutationally Invariant, Reproducing Kernel-Based Potential Energy Surfaces for Polyatomic Molecules: From Formaldehyde to Acetone. *J. Chem. Theory Comput.* **2020**, *16* (9), 5474−5484.
(53) Bartok, A. P.; Payne, M. C.; Kondor, R.; Csanyi, G. Gaussian approximation potentials: the accuracy of quantum mechanics, without the electrons. *Phys. Rev. Lett.* **2010**, *104* (13), 136403.
(54) Xie, Y.; Vandermause, J.; Sun, L.; Cepellotti, A.; Kozinsky, B. Bayesian force fields from active learning for simulation of inter-dimensional transformation of stanene. *npj Comput. Mater.* **2021**, *7* (1), No. 40.
(55) Westermayr, J.; Faber, F. A.; Christensen, A. S.; von Lilienfeld, O. A.; Marquetand, P. Neural networks and kernel ridge regression for

excited states dynamics of $CH_2NH_2^+$: From single-state to multi-state representations and multi-property machine learning models. *Mach. Learn.: Sci. Technol.* **2020**, *1* (2), No. 025009.
(56) Rupp, M.; Tkatchenko, A.; Muller, K. R.; von Lilienfeld, O. A. Fast and accurate modeling of molecular atomization energies with machine learning. *Phys. Rev. lett.* **2012**, *108* (5), No. 058301.
(57) Hansen, K.; Biegler, F.; Ramakrishnan, R.; Pronobis, W.; von Lilienfeld, O. A.; Muller, K. R.; Tkatchenko, A. Machine Learning Predictions of Molecular Properties: Accurate Many-Body Potentials and Nonlocality in Chemical Space. *J. Phys. Chem. Lett.* **2015**, *6* (12), 2326−31.
(58) Hansen, K.; Montavon, G.; Biegler, F.; Fazli, S.; Rupp, M.; Scheffler, M.; von Lilienfeld, O. A.; Tkatchenko, A.; Muller, K. R. Assessment and Validation of Machine Learning Methods for Predicting Molecular Atomization Energies. *J. Chem. Theory Comput.* **2013**, *9* (8), 3404−19.
(59) Qu, C.; Yu, Q.; Bowman, J. M. Permutationally Invariant Potential Energy Surfaces. *Annu. Rev. Phys. Chem.* **2018**, *69*, 151−175.
(60) Behler, J. Atom-centered symmetry functions for constructing high-dimensional neural network potentials. *J. Chem. Phys.* **2011**, *134* (7), No. 074106.
(61) Bartók, A. P.; Kondor, R.; Csányi, G. On representing chemical environments. *Phys. Rev. B Condens Matter* **2013**, *87* (18), 184115.
(62) Christensen, A. S.; Bratholm, L. A.; Faber, F. A.; Anatole von Lilienfeld, O. FCHL revisited: Faster and more accurate quantum machine learning. *J. Chem. Phys.* **2020**, *152* (4), No. 044107.
(63) Pozdnyakov, S. N.; Willatt, M. J.; Bartok, A. P.; Ortner, C.; Csanyi, G.; Ceriotti, M. Incompleteness of Atomic Structure Representations. *Phys. Rev. Lett.* **2020**, *125* (16), 166001.
(64) Blum, L. C.; Reymond, J. L. 970 million druglike small molecules for virtual screening in the chemical universe database GDB-13. *J. Am. Chem. Soc.* **2009**, *131* (25), 8732−3.
(65) Ruddigkeit, L.; van Deursen, R.; Blum, L. C.; Reymond, J. L. Enumeration of 166 billion organic small molecules in the chemical universe database GDB-17. *J. Chem. Inf. Model.* **2012**, *52* (11), 2864−75.
(66) Rupp, M.; Tkatchenko, A.; Muller, K. R.; von Lilienfeld, O. A. Fast and accurate modeling of molecular atomization energies with machine learning. *Phys. Rev. Lett.* **2012**, *108* (5), No. 058301.
(67) Montavon, G.; Rupp, M.; Gobre, V.; Vazquez-Mayagoitia, A.; Hansen, K.; Tkatchenko, A.; Müller, K.-R.; von Lilienfeld, O. A. Machine learning of molecular electronic properties in chemical compound space. *New J. Phys.* **2013**, *15* (9), No. 095003.
(68) Ramakrishnan, R.; Dral, P. O.; Rupp, M.; von Lilienfeld, O. A. Quantum chemistry structures and properties of 134 kilo molecules. *Sci. Data* **2014**, *1*, 140022.
(69) Abreha, B. G.; Agarwal, S.; Foster, I.; Blaiszik, B.; Lopez, S. A. Virtual Excited State Reference for the Discovery of Electronic Materials Database: An Open-Access Resource for Ground and Excited State Properties of Organic Molecules. *J. Phys. Chem. Lett.* **2019**, *10* (21), 6835−6841.
(70) Mai, S.; Marquetand, P.; González, L. A general method to describe intersystem crossing dynamics in trajectory surface hopping. *Int. J. Quantum Chem.* **2015**, *115* (18), 1215−1231.
(71) Westermayr, J.; Gastegger, M.; Menger, M.; Mai, S.; Gonzalez, L.; Marquetand, P. Machine learning enables long time scale molecular photodynamics simulations. *Chem. Sci.* **2019**, *10* (35), 8100−8107.
(72) Axelrod, S.; Shakhnovich, E.; Gómez-Bombarelli, R. Excited state, non-adiabatic dynamics of large photoswitchable molecules using a chemically transferable machine learning potential. *Nat. Commun.* **2022**, *13*, No. 3440.
(73) do Casal, M. T.; Toldo, J. M.; Pinheiro, M.; Barbatti, M. Fewest switches surface hopping with Baeck-An couplings. *Open Res. Eur.* **2021**, *1*, No. 49.
(74) Ishida, T.; Nanbu, S.; Nakamura, H. Clarification of nonadiabatic chemical dynamics by the Zhu-Nakamura theory of nonadiabatic transition: from tri-atomic systems to reactions in solutions. *Int. Rev. Phys. Chem.* **2017**, *36* (2), 229−285.
(75) Yu, L.; Xu, C.; Lei, Y.; Zhu, C.; Wen, Z. Trajectory-based nonadiabatic molecular dynamics without calculating nonadiabatic coupling in the avoided crossing case: trans<−>cis photoisomerization in azobenzene. *Phys. Chem. Chem. Phys.* **2014**, *16* (47), 25883−95.
(76) Shchepanovska, D.; Shannon, R. J.; Curchod, B. F. E.; Glowacki, D. R. Nonadiabatic Kinetics in the Intermediate Coupling Regime: Comparing Molecular Dynamics to an Energy-Grained Master Equation. *J. Phys. Chem. A* **2021**, *125* (16), 3473−3488.
(77) Yue, L.; Yu, L.; Xu, C.; Lei, Y.; Liu, Y.; Zhu, C. Benchmark Performance of Global Switching versus Local Switching for Trajectory Surface Hopping Molecular Dynamics Simulation: Cis<−>Trans Azobenzene Photoisomerization. *ChemPhysChem* **2017**, *18* (10), 1274−1287.
(78) Yue, L.; Yu, L.; Xu, C.; Zhu, C.; Liu, Y. Quantum yields of singlet and triplet chemiexcitation of dimethyl 1,2-dioxetane: ab initio nonadiabatic molecular dynamic simulations. *Phys. Chem. Chem. Phys.* **2020**, *22* (20), 11440−11451.
(79) Lier, B.; Poliak, P.; Marquetand, P.; Westermayr, J.; Oostenbrink, C. BuRNN: Buffer Region Neural Network Approach for Polarizable-Embedding Neural Network/Molecular Mechanics Simulations. *J. Phys. Chem. Lett.* **2022**, *13* (17), 3812−3818.
(80) Westermayr, J.; Chaudhuri, S.; Jeindl, A.; Hofmann, O. T.; Maurer, R. J. Long-range dispersion-inclusive machine learning potentials for structure search and optimization of hybrid organic−inorganic interfaces. *Digital Discovery* **2022**, DOI: 10.1039/D2DD00016D.
(81) Kingma, D. P.; Ba, J. L. Adam: A Method for Stochastic Optimization. *arXiv (Computer Science.Machine Learning)*, January 30, 2017, 1412.6980, ver. 9. https://arxiv.org/abs/1412.6980 (accessed 2022-05-09).
(82) Goodfellow, I.; Bengio, Y.; Courville, A. *Deep Learning*; MIT Press, 2016.
(83) Hastie, T.; Tibshirani, R.; Friedman, J. H. *The Elements of Statistical Learning: Data Mining, Inference, and Prediction*, 2nd ed.; Springer: New York, 2009.
(84) Bishop, C. M. *Pattern Recognition and Machine Learning*, 1st ed.; Springer: New York, 2006.
(85) Kästner, J. Umbrella sampling. *Wiley Interdiscip. Rev.: Comput. Mol. Sci.* **2011**, *1* (6), 932−942.
(86) Tao, G. Trajectory-guided sampling for molecular dynamics simulation. *Theor. Chem. Acc.* **2019**, *138* (3), No. 34.
(87) Yang, Y. I.; Shao, Q.; Zhang, J.; Yang, L.; Gao, Y. Q. Enhanced sampling in molecular dynamics. *J. Chem. Phys.* **2019**, *151* (7), No. 070902.
(88) Herr, J. E.; Yao, K.; McIntyre, R.; Toth, D. W.; Parkhill, J. Metadynamics for training neural network model chemistries: A competitive assessment. *J. Chem. Phys.* **2018**, *148* (24), 241710.
(89) Shang, C.; Liu, Z. P. Stochastic Surface Walking Method for Structure Prediction and Pathway Searching. *J. Chem. Theory Comput.* **2013**, *9* (3), 1838−45.
(90) Dahl, J. P.; Springborg, M. The Morse oscillator in position space, momentum space, and phase space. *J. Chem. Phys.* **1988**, *88* (7), 4535−4547.
(91) Smith, J. S.; Isayev, O.; Roitberg, A. E. ANI-1: an extensible neural network potential with DFT accuracy at force field computational cost. *Chem. Sci.* **2017**, *8* (4), 3192−3203.
(92) Barbatti, M.; Sen, K. Effects of different initial condition samplings on photodynamics and spectrum of pyrrole. *Int. J. Quantum Chem.* **2016**, *116* (10), 762−771.
(93) Zhu, X.; Thompson, K. C.; Martinez, T. J. Geodesic interpolation for reaction pathways. *J. Chem. Phys.* **2019**, *150* (16), 164103.
(94) Avagliano, D.; Lorini, E.; González, L. Sampling effects in quantum mechanical/molecular mechanics trajectory surface hopping non-adiabatic dynamics. *Philos. Trans. R. Soc. A* **2022**, *380* (2223), 20200381.
(95) Behler, J. Constructing high-dimensional neural network potentials: A tutorial review. *Int. J. Quantum Chem.* **2015**, *115* (16), 1032−1050.

(96) Cox, J. M.; Bain, M.; Kellogg, M.; Bradforth, S. E.; Lopez, S. A. Role of the Perfluoro Effect in the Selective Photochemical Isomerization of Hexafluorobenzene. *J. Am. Chem. Soc.* **2021**, *143* (18), 7002−7012.
(97) Haller, I. Photoisomerization of Hexafluorobenzene. *J. Am. Chem. Soc.* **1966**, *88* (9), 2070−2071.
(98) Mukherjee, S.; Pinheiro, M., Jr.; Demoulin, B.; Barbatti, M. Simulations of molecular photodynamics in long timescales. *Philos. Trans. R. Soc. A* **2022**, *380* (2223), 20200382.

https://doi.org/10.1021/acs.accounts.2c00288
Acc. Chem. Res. 2022, 55, 1972−1984